JACS Au
AN OPEN ACCESS JOURNAL OF THE AMERICAN CHEMICAL SOCIETY

pubs.acs.org/jacsau
Article

Engineering Unsaturated Cu_1-O_3 Coordination to Boost Oxygen Species Activation for Low-Temperature Catalysis in CO Oxidation

Yadi Wang,[¶] Zeyu Jiang,[¶] Fan Dang,[¶] Chaoqian Ai, Jialei Wan, Chunli Ai, Yani Wu, Chi Ma, Mingjiao Tian, Han Xu, Reem Albilali, Weisheng Guan, Hongna Zhang,* and Chi He*

Cite This: *JACS Au* 2025, 5, 1677−1688
Read Online

ACCESS | Metrics & More | Article Recommendations | Supporting Information

ABSTRACT: The activation of lattice oxygen at low temperatures is essential for heterogeneous catalytic oxidation, but exactly how this is achieved by adjusting the coordination structure of atomic sites is still elusive. Herein, the $Cu_1O_3-CeO_2$ catalyst with highly dispersed unsaturated Cu_1-O_3 coordination was creatively engineered, which remarkably enhanced the low-temperature oxidation of CO (a typical model reaction) from 12% to 90% at 66 °C compared to conventional $CuCeO_x$ catalyst. The preservation of atomic coordination-deficient Cu sites enables the transfer of electron cloud density from Cu atoms to O atoms, hence, facilitating the activation of lattice oxygen. Further electron transfer from O atom to Cu species results in charge back-donation to form sufficient Cu^+ and metal per-oxy species, contributing to weaken O−O bonds. We determined that the increasing number of electron donors induced by unsaturated atomic Cu_1-O_3 coordination is an efficient strategy to develop highly active and stable catalysts for lattice oxygen activation. The catalyst synthesis strategies and oxygen activation mechanism demonstrated in this work provide a generalizable platform for the future design of well-defined functional catalysts for low-temperature oxidation reactions.

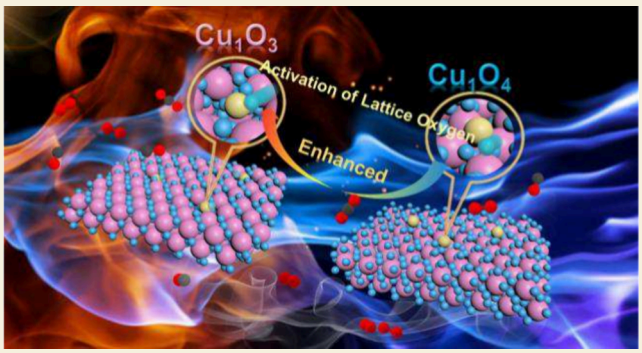

KEYWORDS: *Lattice oxygen activation, Charge back-donation, Coordination-unsaturated sites, Electronic structure, Low-temperature oxidation*

INTRODUCTION

The efficiency of catalytic reactions is primarily determined by the electronic configuration of the active sites.[1−3] These electronic configurations can be precisely modulated by optimizing the metal/metal-oxide support interfacial interactions, which in-turn can affect the coordination environments of metal centers, ultimately regulating electronic reconfigurations of the active site centers for a better charge transfer.[4] In addition to the inherent electronic properties of catalysts, several other key aspects such as strong bonding for improved metal−support interactions and synergistic effects between individual components of composite materials for enhanced interfacial effect should also be considered.[5−7] For instance, the electronic configuration of the metal doped metal-oxide catalyst can be regulated to transfer charge and control the ratio of redox pairs efficiently.[8,9] Meanwhile, the activated lattice oxygen species can directly engage in the reaction during heterogeneous catalytic oxidation. Lattice oxygen is sequestered within the catalyst's crystal structure by adjacent atoms or ions, hindering direct interaction with the reactant molecules. Beyond that, lattice oxygen activation often requires overcoming a high energy barrier. Reasonable control of lattice oxygen activity on metal oxide surfaces remains a great challenge. Through the appropriate modulation of the electronic structure of catalyst, the activation of lattice oxygen can be effectively promoted.[10−12] The activation capacity of lattice oxygen species can be modulated by adjusting the unoccupied *d*-band center, *s*-band filling, and *d*-band filling.[13,14] These modifications can effectively promote lattice oxygen migration and oxygen vacancy formation by reducing the formation energy. In addition, restructuring the electronic structure of catalyst to regulate the formation of unique coordination structures for the active center will promote electron transfer efficiency, and weaken the oxygen bond strength of the metal lattice to improve the reactivity of lattice oxygen species.[15,16] The manipulation of these factors for enhanced catalytic activity presents significant opportunities for future research.

Received: November 27, 2024
Revised: February 2, 2025
Accepted: February 3, 2025
Published: April 15, 2025

https://doi.org/10.1021/jacsau.4c01149
JACS Au 2025, 5, 1677−1688

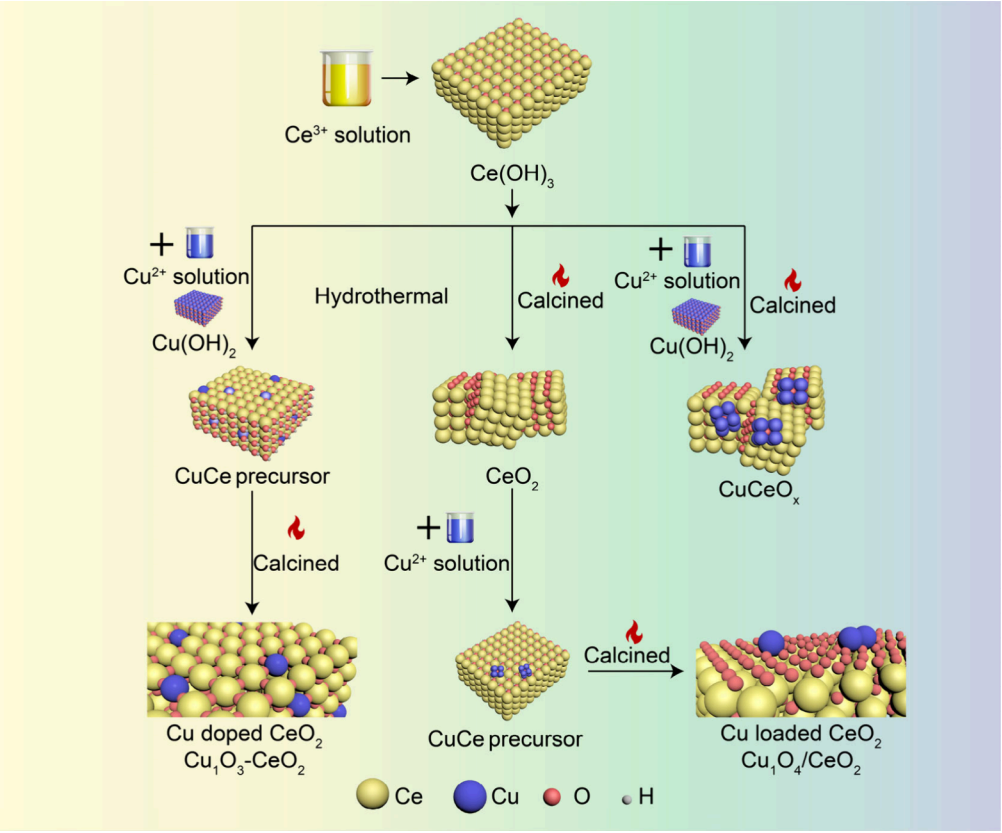

Figure 1. Schematic illustration for synthesizing the copper−ceria catalysts.

In the last few decades, the copper−ceria catalysts have been extensively explored for various catalytic reactions.[17−20] However, the majority of these studies focused on ceria as support and copper nanoparticles as supported active sites; whereas, the core atomic structure of the active site in the copper−ceria catalyst has remained largely unexplored. The unique Cu/CeO_2 electronic and chemical properties have been well established by several reports. It is generally accepted that the strong metal−support interactions through the formation of bonds between the Cu−[O]−Ce interfaces significantly enhances the catalytic activity.[21] Wang et al. reported that except for the Cu−[O_x]−Ce (x = 0.7−3.2) structure, the highly dispersed CuO_x (x = 0.2−0.5) cluster was the crucial active species.[22] Moreover, the CuO_x clusters were easily reduced to Cu(I) species when they were subjected to CO.[23] Another study indicated that the CO catalytic oxidation efficiency of the isolated Cu(I)/(II) sites were ten times higher than that of CuO clusters.[24] Similarly, in another report, it was proposed that a higher concentration of oxygen vacancies on the catalyst surface provided additional bonding sites for Cu^+;[25] whereas, a parallel study suggested that Cu^{3+}/Cu^{2+}−O−Ce redox centers remained equally active as those in $Cu_xCe_{1-x}O_2$ solid solutions rather than Cu^+ or Cu^{2+} during CO oxidation.[26−28] The Yu and Chen groups found that different coordination copper species with various coordination states displayed different catalytic activity based on the strong or weak metal−support bonding to achieve a different CO oxidation activity.[29,30] The results indicated an urgent necessity to comprehensively investigate the correlation between the coordination structures of active sites and their catalytic behaviors for the development of effective copper−ceria catalysts.

Herein, a variety of catalysts were carefully synthesized with distinct bonding types between Cu and Ce atoms, resulting in different coordination of Cu sites. In depth experimental studies coupled with DFT calculations demonstrated that the atomic dispersed Cu atoms with an unsaturated coordination state lead to varying degrees of charge transfer, which subsequently modifies the metal active sites for the improved adsorption and transformation efficiency. Furthermore, the formation of unsaturated coordination $Cu_1−O_3$ results in sufficient surface-activated lattice oxygens adjacent to Cu sites, which actively engages in the reaction with reduced free energy. The creation of highly scattered and unsaturated Cu coordination sites along with elucidating their critical functions should yield valuable insights for the rational design of coordination-regulated engineering and the synthesis of highly active catalysts for heterogeneous oxidation.

EXPERIMENTAL SECTION

Catalyst Preparation

The CeO_2 was prepared by a hydrothermal method, and the Cu-CeO_2 catalyst was synthesized using a one-pot method. The Cu/CeO_2 catalyst was prepared through a general impregnation method. The $CuCeO_x$ catalyst was synthesized by calcining mixtures of $Ce(OH)_3$ and $Cu(OH)_2$ precursors via mechanical grinding. Additional details for catalyst preparation are provided in the Supporting Information.

Characterizations and Theoretical Calculations

The catalysts were characterized by X-ray diffraction (XRD), inductively coupled plasma optical emission spectrometry (ICP-OES), high-resolution transmission electron microscopy (HR-TEM), energy dispersive spectroscopy (EDS) mapping, X-ray photoelectron spectroscopy (XPS), ultraviolet−visible spectroscopy spectra (UV−

https://doi.org/10.1021/jacsau.4c01149
JACS Au 2025, 5, 1677−1688

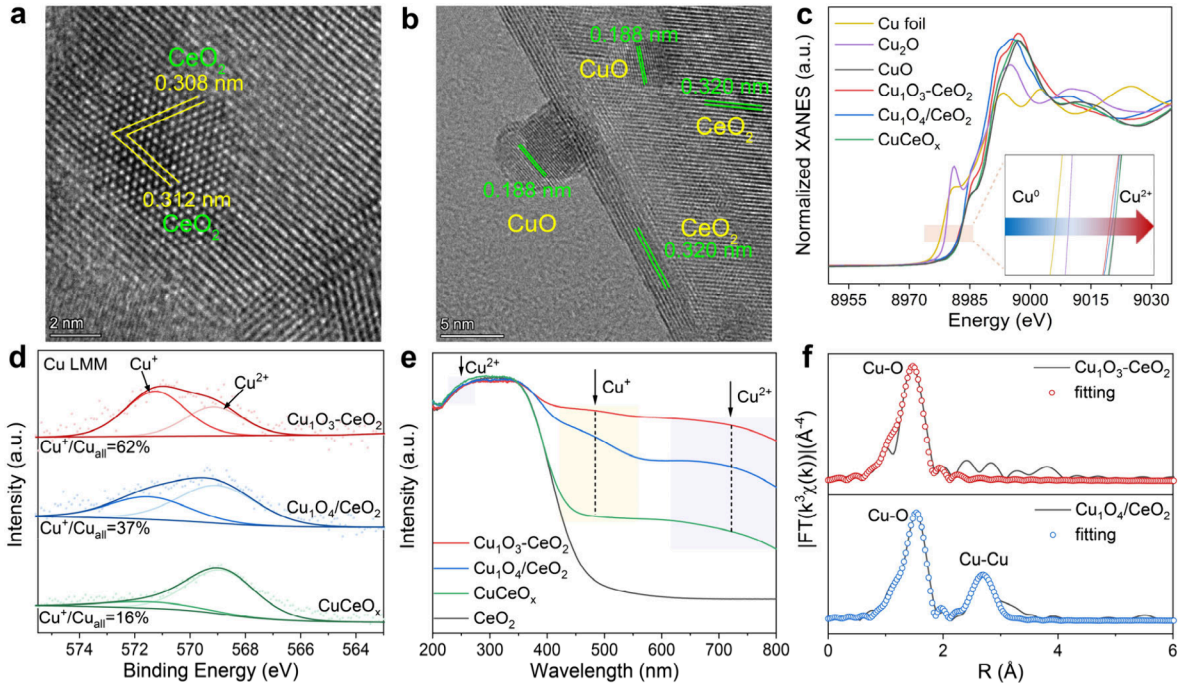

Figure 2. (a, b) Corresponding HR-TEM images of Cu_1O_3−CeO_2 and Cu_1O_4/CeO_2 catalysts. (c) XANES spectra, (d) Cu LMM XPS, and (e) UV−Vis absorption spectra of prepared catalysts. (f) EXAFS spectra of Cu_1O_3−CeO_2 and Cu_1O_4/CeO_2 catalysts.

Vis), X-ray absorption fine structure spectra (XAFS), electron paramagnetic resonance (EPR), Raman spectroscopy, temperature-programmed desorption of oxygen (O_2-TPD), temperature-programmed reduction of CO (CO-TPR), temperature-programmed reduction of hydrogen (H_2-TPR), temperature-programmed desorption of CO (CO-TPD), *in situ* diffuse reflectance infrared Fourier transform spectroscopy of CO adsorption (CO−DRIFTS), *in situ* diffuse reflectance infrared Fourier transform spectroscopy (DRIFTS), operando near ambient pressure X-ray photoelectron spectroscopy (NAP-XPS), and ^{18}O isotopic labeling experiment. The Vienna Ab-initio Simulation Package (VASP) was employed to perform all the density functional theory (DFT) calculations within the generalized gradient approximation (GGA) using the Perdew, Burke, and 0 (PBE) formulation. The detailed procedures are described in the Supporting Information.

RESULTS AND DISCUSSION

Structural and Surface Characteristics

Three different processes were employed to synthesize site-specific copper−ceria catalysts, including *in situ* doping (denoted as Cu_1O_3−CeO_2), impregnation (denoted as Cu_1O_4/CeO_2), and calcination of hydroxide precursor mixtures (denoted as $CuCeO_x$) (Figure 1). The crystalline structures of the prepared catalysts were determined by powder X-ray diffraction (XRD). Figure S1 indicates that all obtained catalysts, even after Cu doping, maintain the crystalline phase of the fluorite CeO_2 structure (PDF#34-0349). Meanwhile, an additional weaker diffraction peak is observed in the Cu_1O_4/CeO_2 catalyst, which can be assigned to the CuO crystalline phase (PDF#45-0937). However, CuO characteristic peaks are observed in the $CuCeO_x$ catalyst obviously. The actual Cu content of catalysts (≈3.2−3.3 wt %) was identified by inductively coupled plasma optical emission spectrometry (ICP-OES), as shown in Table S1.

The high-resolution transmission electron microscopy (HR-TEM) images show that the copper−ceria catalysts possess three different morphologies. The Cu_1O_3−CeO_2 nanocubes with an average size of 10−20 nm show interplanar lattice fringes of 0.308 and 0.312 nm, assigned to the {111} plane of fluorite CeO_2 (Figures S2a,b and 2a). The narrowing of the interplanar lattice fringes of the {111} plane compared to Cu_1O_4/CeO_2 and pure CeO_2 is attributed to the lattice distortion caused by doping effects (Figures 2b and S3b). The Cu_1O_4/CeO_2 catalyst presents a coexistence of nanoparticles and nanorods, and the support maintains the lattice fringe of the original {111} plane of CeO_2 (Figures 2b, S2c,d). Furthermore, apart from clear CeO_2 lattice fringes, CuO lattice fringes belonging to {002} plane with 0.247 nm are also observed over the $CuCeO_x$ ultrasmall particles (Figure S4c). The corresponding energy dispersive spectroscopy (EDS) mapping confirms the homogeneous spatial distribution of Cu and Ce in the Cu_1O_3−CeO_2 catalyst, which indicates that the Cu species is well-dispersed and successfully incorporated (Figure S5a). However, large particles of CuO are observed in Figure S 4d.

The valence states of Cu in three catalysts were verified by Cu LMM and Cu 2*p* X-ray photoelectron spectroscopy (XPS). The Cu 2*p* spectra can be deconvoluted to Cu $2p_{1/2}$ and Cu $2p_{3/2}$ regions (Figure S6).[31−33] Specifically, the peaks centered around 932.5 and 952.1 eV are assigned to the Cu^+ species; whereas, the peaks of 934.3 and 954.0 eV can be assigned to the Cu^{2+} species. It is worth noting that the ratio of Cu^+ species decreases with the sequence Cu_1O_3−CeO_2 > Cu_1O_4/CeO_2 > $CuCeO_x$. Furthermore, the higher proportion of Cu^+ species (571.2 eV) over the Cu_1O_3−CeO_2 ($Cu^+/(Cu^+ + Cu^{2+})$ = 62%) sample as evidenced by Cu LMM, consistent with Cu 2*p* results, confirms a change in the structure resulting from the replacement of atomic Ce by Cu ions (Figure 2d).[34−36]

The chemical state of the Cu species over the CeO_2 support was further verified by ultraviolet−visible spectroscopy (UV−Vis) spectra of the catalysts (Figure 2e). A weak and broad absorption at ∼720 nm is assigned to the $2E_g \rightarrow 2T_{2g}$ spin-allowed *d-d* transitions of the Cu (II) in the Cu species,[37]

https://doi.org/10.1021/jacsau.4c01149
JACS Au 2025, 5, 1677−1688

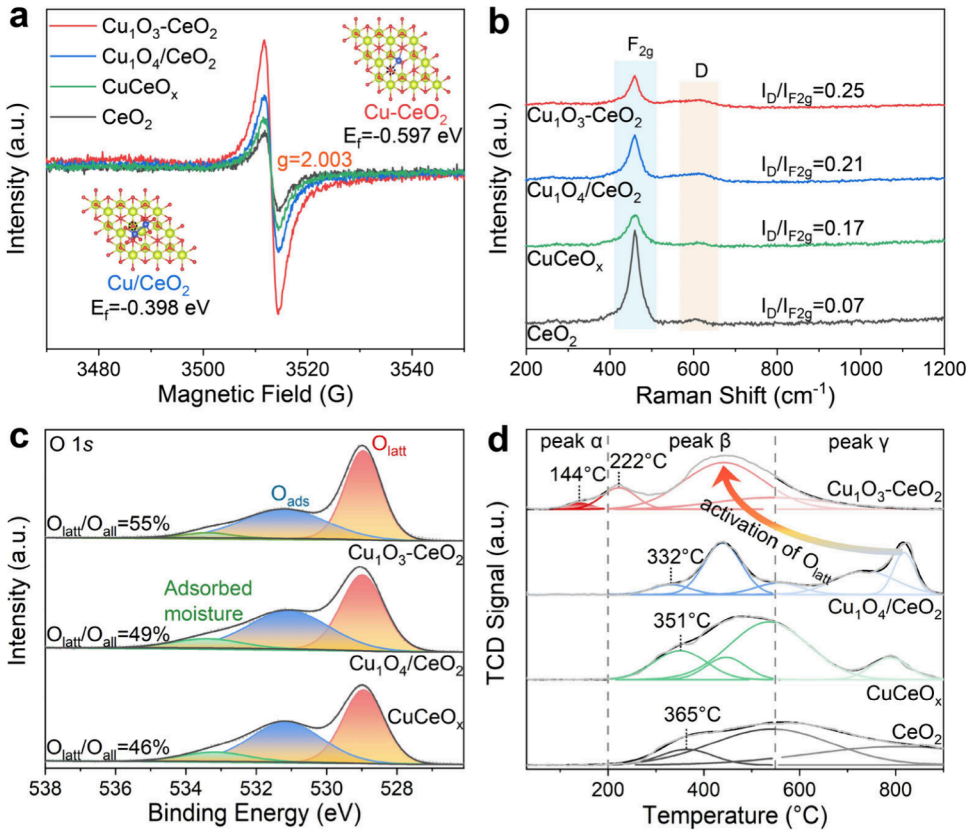

Figure 3. (a) EPR spectra and calculated oxygen vacancy formation energy of Cu_1O_3−CeO_2 and Cu_1O_4/CeO_2 catalysts; color code: Ce (Green), O (red), and Cu (blue); black dotted line indicates the oxygen vacancy sites. (b) Raman spectra of prepared catalysts. (c) O 1*s* spectra and (d) O_2-TPD profiles of prepared catalysts.

which can be observed in all Cu-containing samples. Here, $CuCeO_x$ was observed to exhibit obvious peaks of Cu^{2+}. An additional peak (253 nm) corresponding to CuO_x over Cu_1O_4/CeO_2 and $CuCeO_x$ catalyst can also be observed.[38−41] We determined that the aggregated CuO_x is more challenging in converting to Cu_2O species than the dispersed CuO species under the same conditions. Meanwhile, a new peak located at 450 nm due to the emergence of Cu_2O is also observed in both Cu_1O_3−CeO_2 and Cu_1O_4/CeO_2 catalysts, confirming the existence of Cu^+ sites in these two catalysts.[42]

The X-ray absorption fine structure (XAFS) spectra were subsequently adopted to detect the coordination states of Cu atoms. The Cu K-edge of the X-ray absorption near-edge structure (XANES) plots for the CuCe catalysts with the edge energy of 8980−8985 eV was located between reference samples of Cu_2O and CuO, indicating the Cu species are maintained in mixed valence state between Cu(I) and Cu(II), as shown in Figure 2c. When the absorption edge is closer to the higher energy region, its valence state is higher.[43,44] The average valence state of the Cu species for three catalysts is increased with the sequence of Cu(I) < Cu_1O_3−CeO_2 < Cu_1O_4/CeO_2 < $CuCeO_x$ < Cu(II), and the Cu K-edge in $CuCeO_x$ is almost overlapped with that in CuO, which is consistent with the XPS and UV−Vis results. This phenomenon can be attributed to the dispersion and coordination structures of the catalysts' active sites. The representative catalysts were further analyzed by extended X-ray absorption fine structure (EXAFS) to probe their bonding types. As displayed in Figures 2f and S7, the only apparent peak around 1.93 Å can be detected and ascribed to the scattering path of the Cu−O bond in Cu_1O_3−CeO_2, without chemically bonded Cu−Cu, which proves that the Cu species exist in a well-dispersed atomic form. The additional smaller peak at 2.98 Å, assigned to the Cu−Cu scattering at the second shell of Cu_1O_4/CeO_2 is evidently attributed to the formation of CuO particles, in accordance with the XRD results. Moreover, the peak of $CuCeO_x$ at the second shell demonstrated the presence of CuO particles. The EXAFS fitting curves reveal that the unsaturated coordination Cu_1−O_3 configuration existed in Cu_1O_3−CeO_2, while the Cu_1−O_4 configuration existed in Cu_1O_4/CeO_2 and $CuCeO_x$. The corresponding Cu−O bond coordination numbers (CN) of Cu_1O_3−CeO_2, Cu_1O_4/CeO_2 and $CuCeO_x$ are about 3.2, 3.7 and 3.8, respectively (Table S2). Combined with the above results, this study focused on the represented Cu_1O_3−CeO_2 and Cu_1O_4/CeO_2 catalysts for an in-depth exploration. To confirm the rationality of the coordination structure for Cu_1O_3−CeO_2 and Cu_1O_4/CeO_2 catalysts, we calculated the surface potential energies by theoretical calculations (Figure S8). The results indicate that the formation of Cu_1O_3−CeO_{22} exhibits the lowest surface potential energy, confirming the congruence of the local structures with the EAXFS findings.

The Ce 3*d* XPS spectra can be deconvoluted into ten peaks, as shown in Figure S9. The four peaks (u′, u_0, v′, and v_0) are assigned to the surface Ce^{3+} species.[45,46] The stronger intensity of Ce^{3+} peaks verifies that a substantial amount of oxygen vacancies is introduced into CeO_2 during the incorporation of copper species. The calculated $Ce^{3+}/(Ce^{3+} + Ce^{4+})$ ratio of catalysts follows the order of Cu_1O_3−CeO_2 > Cu_1O_4/CeO_2 > $CuCeO_x$ > CeO_2. It has been reported that the transition metal

https://doi.org/10.1021/jacsau.4c01149
JACS Au 2025, 5, 1677−1688

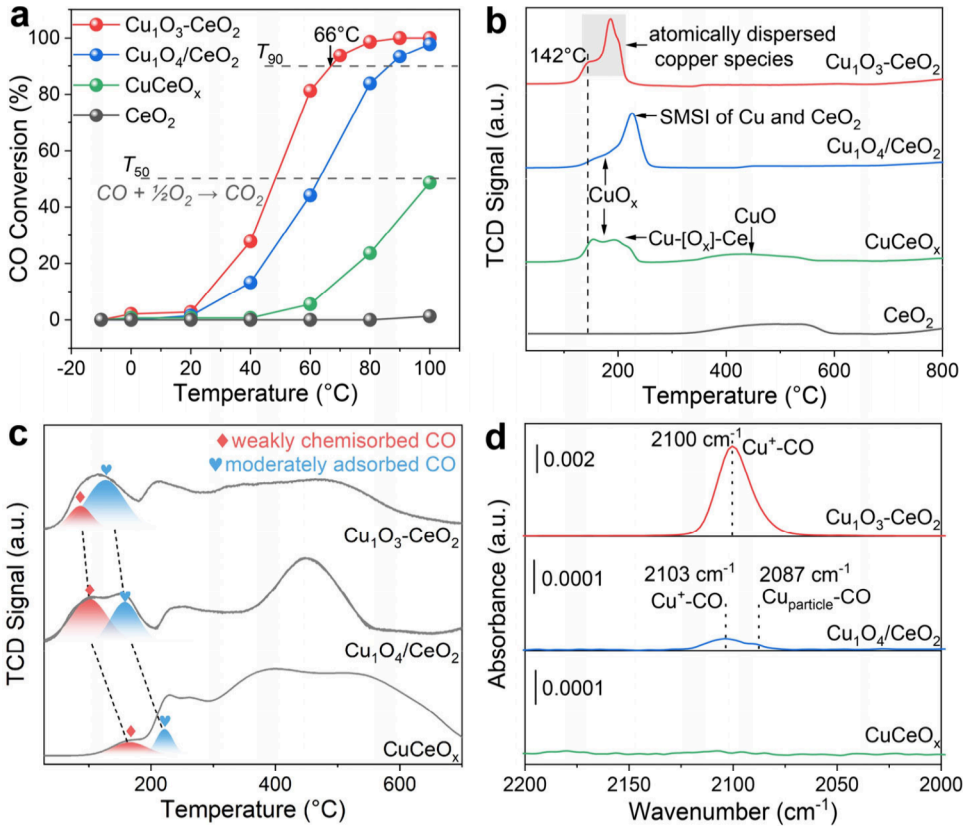

Figure 4. (a) Catalytic activity evaluation of CO oxidation over prepared catalysts. (b) H_2-TPR profiles, (c) CO-TPD profiles, and (d) DRIFT spectra of CO adsorption over prepared catalysts.

doped CeO_2 can result in the formation of oxygen vacancies, which was further verified by the electron paramagnetic resonance (EPR) results.[46,47] The EPR of the Cu_1O_3−CeO_2 catalyst shows a strong signal of trapped electrons in oxygen vacancies (g = 2.003; Figure 3a). Additionally, Raman spectroscopy was used to monitor the concentration of oxygen vacancies in the samples (Figure 3b). The relative peak intensity ratio (I_D/I_{F2g}) between the defect-induced (D) mode peak (~605 cm^{-1}) and F_{2g} symmetry mode peak (~459 cm^{-1}) pose positive relationship to the concentration of oxygen vacancy in CeO_2.[48] The I_D/I_{F2g} value increases from 0.07 to 0.25 with the introduction of Cu, indicating an increasing of charge-compensating oxygen vacancies. Moreover, the Cu_1O_4/CeO_2 also exhibits an increased number of oxygen vacancies, which may due to the electron transfer from the Cu species to the CeO_2 support.[49] Density functional theory (DFT) simulations were performed to calculate the formation energy (E_f) of the oxygen vacancy on the Cu_1O_3−CeO_2 and Cu_1O_4/CeO_2 catalyst surface (Figure 3a). Both Cu_1O_3−CeO_2 and Cu_1O_4/CeO_2 can create oxygen vacancies spontaneously at the sites near the Cu species. Cu_1O_3−CeO_2 possesses a relatively lower oxygen vacancy formation energy (−0.597 eV) as lattice oxygen near the unsaturated coordination of the Cu species can be activated efficiently.

The O 1*s* peaks located at 533.4, 531.2, and 528.9 eV are ascribed to the adsorbed H_2O molecules, surface adsorbed oxygen and lattice oxygen, respectively (Figure 3c).[50−52] The O_{latt} among all oxygen species of Cu_1O_3−CeO_2 with a ratio of 55% is higher than those of Cu_1O_4/CeO_2 (49%) and $CuCeO_x$ (46%). The adsorption capability of catalysts toward O_2 molecules was further evaluated by the temperature-programmed desorption of oxygen (O_2-TPD) (Figure 3d). Only Cu_1O_3−CeO_2 exhibits a significantly high oxygen release process from physically adsorbed oxygen below 200 °C compared to the Cu_1O_4/CeO_2 and $CuCeO_x$ catalysts, proving that it has better oxygen adsorption capacity. Meanwhile, no desorption peaks can be detected at high temperatures over the Cu_1O_3−CeO_2 catalyst, indicating its excellent O_{latt} transferring and activating ability. A negative peak below 200 °C for Cu−Ce catalysts is observed due to the desorption of CO from CeO_2, as shown in the temperature-programmed reduction of CO (CO-TPR) patterns (Figure S10).[53] A strong CO consumption peak of Cu_1O_3−CeO_2, Cu_1O_4/CeO_2 and $CuCeO_x$ catalysts were detected at around 254, 272, and 321 °C, respectively, attributing to the oxidation of CO by surface lattice oxygen of Cu−Ce catalysts. Here, we propose that atomically dispersed Cu species embedded in the CeO_2 lattice interstice can cause lattice distortion and lead to induction of more surface defects. We suppose that the strong electron-donating property of the Cu particles alters the structural reactivity, resulting in a higher ability to activate and dissociate O_{latt} and molecular oxygen.

Catalytic Performance and Properties

The activity of the prepared catalysts was assessed by employing temperature-programmed CO oxidation as the model reaction. As shown in Figure 4a, the catalytic activity of the pure CeO_2 support is negligible, which confirms that the Cu species as active sites play a vital role in CO oxidation at low temperatures. Both Cu_1O_3−CeO_2 and Cu_1O_4/CeO_2 catalysts exhibit CO oxidation reactivity even at room temperature. Moreover, the T_{50} (the temperature of 50% CO conversion) turns out to be 48 and 63 °C for the Cu_1O_3−

https://doi.org/10.1021/jacsau.4c01149
JACS Au 2025, 5, 1677−1688

CeO_2 and Cu_1O_4/CeO_2 catalysts, respectively. Contrastingly, $CuCeO_x$ only achieves 48% conversion of CO even at a higher temperature of 100 °C. Interestingly, the lowest T_{90} (the temperature of 90% CO conversion) is obtained from the $Cu_1O_3-CeO_2$ catalyst at 66 °C. The catalytic performance is not affected even if the WHSV is increased (Figure S11). These results demonstrate that the effectiveness of these catalysts is directly related to the atomic locations of Cu species. Furthermore, the CO oxidation kinetics were measured by the Arrhenius plots based on aforementioned data. As shown in Figure S12, the $Cu_1O_3-CeO_2$ catalyst exhibits the lowest apparent activation energy (E_a; ~ 45 kJ·mol^{-1}) compared to those of Cu_1O_4/CeO_2 (~71 kJ·mol^{-1}) and $CuCeO_x$ (~91 kJ·mol^{-1}) samples.

Redox properties of the catalysts were further determined by the temperature-programmed reduction of hydrogen (H_2-TPR) to investigate the reason behind such differences in apparent activation energy. As depicted in Figure 4b, the main reduction peak of the $Cu_1O_3-CeO_2$ catalyst shifts to a lower temperature (186 °C, with a small shoulder peak at around 142 °C) in comparison to the other catalysts. The two adjacent sharp reduction peaks at temperatures below 200 °C are assigned to the presence of atomically dispersed copper species.[29] For Cu_1O_4/CeO_2, the main reduction peak around 225 °C is assigned to the strong metal−support interaction (SMSI) between Cu and the CeO_2 support, leading to a rise in the reduction temperature due to the strong bonding. A broad reduction peak at 150−225 °C in the $CuCeO_x$ catalyst is attributed to the highly dispersed CuO_x and Cu-[O_x]-Ce solid solution structure. The H_2-TPR of CuO in Figure S13 is taken as a reference, the CuO reduction temperature remains above 300 °C. Based on these results, it can be postulated that the different types of binding between copper and CeO_2 using different synthetic methods result in diverse interactions, which further lead to significant discrepancy in catalytic performance. Notably, the synthesized Pt/CeO_2 and Au/CeO_2 (kept with the same loading amount) and TM-CeO_2 (other transition metals doped CeO_2) exhibit much lower performance compared to the $Cu_1O_3-CeO_2$ catalysts for CO oxidation (Figures S14 and S15). These results further confirm that atomically dispersed and coordination-unsaturated copper species significantly promote the catalytic performance. Additionally, CuO nanoparticles were detected while increasing the Cu content during $Cu_1O_3-CeO_2$ catalyst synthesis, but no enhancement of the catalytic performance is observed (Figures S16 and S17). It has been shown that just a particular degree of doping causes the catalyst to generate stable Cu_1O_3 sites and promotes lattice oxygen activation near the active sites, hence, maximizing performance. The surplus CuO on the surface does not function as the active site in this system and fails to entirely obscure the Cu species that have been incorporated into the lattice. The prior active sites consist of unsaturated coordinated Cu species with doped segments, which are abundant and robust enough to maintain catalytic efficiency. Therefore, we claim that the surface segregation of Cu atoms caused by the excessive doping can lead to the formation of CuO, but could not further enhance the catalytic performance.

For practical applications, the stability of the catalysts is of crucial importance. Therefore, the stability of the prepared $Cu_1O_3-CeO_2$ and Cu_1O_4/CeO_2 samples were assessed by the H_2O resistance test between a heating and cooling cycle (Figure S18). It is observed that the presence of water vapor reduced the CO oxidation performance. For the feed of 3 vol % H_2O, the performance of $Cu_1O_3-CeO_2$ and Cu_1O_4/CeO_2 decreases by 18−19% and 22−23%, respectively, which may be due to the competitive adsorption between H_2O molecules and reactants.[4] Furthermore, we recorded the temperature-programmed desorption of the CO (CO-TPD) profiles of Cu−Ce catalysts to investigate their CO adsorption ability. As shown in Figure 4c, the desorption peaks around 86, 99, and 166 °C correspond to the weakly chemisorbed CO on the surface, which does not participate in the CO oxidation reaction. The moderately adsorbed CO species shown in Figure 4c supposedly plays an important role in CO oxidation.[54] The CO desorption temperatures for the $Cu_1O_3-CeO_2$, Cu_1O_4/CeO_2, and $CuCeO_x$ catalysts are determined as 127, 158, and 222 °C, respectively. The peak position of the CO desorption for $Cu_1O_3-CeO_2$ catalyst considerably shifts to the lower temperature compared with the desorption peaks of Cu_1O_4/CeO_2 and $CuCeO_x$ catalysts, indicating that the adsorption capacity of $Cu_1O_3-CeO_2$ is superb as compared to other catalysts, consistent with the catalytic activity results. These observations verify that various coordination structures between Cu and Ce result in diverse absorption and activation abilities toward CO molecules on the Cu active sites. DFT calculation on copper species also confirms that $Cu_1O_3-CeO_2$ possesses a lower CO adsorption energy (−1.087 eV), and therefore, it tends to adsorb and activate more CO compared with that of Cu_1O_4/CeO_2 (Figure S19).

In order to further understand the CO adsorption behavior on active Cu species, we perform *in situ* diffuse reflectance infrared Fourier transform spectroscopy (DRIFTS) experiments at 25 °C (Figures 4d and S20). Figure S20 displays the CO−DRIFTS spectra recorded during the adsorption process, revealing the peaks at 2170 and 2113 cm^{-1} corresponding to gaseous CO adsorption on CeO_2.[55,56] Additionally, the CO adsorption peak for $Cu_1O_3-CeO_2$ shifts to 2104 cm^{-1}, indicating increased CO adsorption on Cu^+. To resolve peak overlap, weaker CO adsorbed on CeO_2 was removed by purging, revealing a peak at ~2100 cm^{-1} attributed to linearly adsorbed CO on Cu^+. This peak is observed in both $Cu_1O_3-CeO_2$ and Cu_1O_4/CeO_2 (Figure 4d).[23,29] However, the intensity of the Cu^+-CO signal decreases gradually as the CeO_2 surface is increasingly covered by the Cu nanoparticles. Evidently, the CO adsorption behavior on $Cu_1O_3-CeO_2$ is much stronger than that on Cu_1O_4/CeO_2, attributing to the strong chemisorbed CO on Cu^+ species in an electron-deficient state induced by Cu−O coordination. The results unambiguously confirm the atomic dispersion of Cu^+ in $Cu_1O_3-CeO_2$. Interestingly, compared to the $Cu_1O_3-CeO_2$ sample (2100 cm^{-1}), a remarkable red shift of the linear-bonded CO peak on the Cu site is observed in Cu_1O_4/CeO_2 (2103 cm^{-1}), indicating that electronegativity of Cu species was enhanced in the $Cu_1O_3-CeO_2$ sample. It is hypothesized that the electron feedback from Cu to the CO $2\pi^*$ antibonding orbital was enhanced due to the electron transfer from Ce to Cu. This transfer leads to a reduction in the bond order of CO. An additional weak peak at 2087 cm^{-1}, assigned to Cu particle-CO, was also observed in the Cu_1O_4/CeO_2 spectrum, revealing that the adsorption behavior of CO on Cu_1O_4/CeO_2 can be determined by Cu^+ on the interface. Moreover, the linearly bonded CO peak was not detected in the CO-DRIFTS spectra for $CuCeO_x$. Furthermore, the variation trend of CO adsorption behavior is highly consistent with that of the CO

https://doi.org/10.1021/jacsau.4c01149
JACS Au 2025, 5, 1677−1688

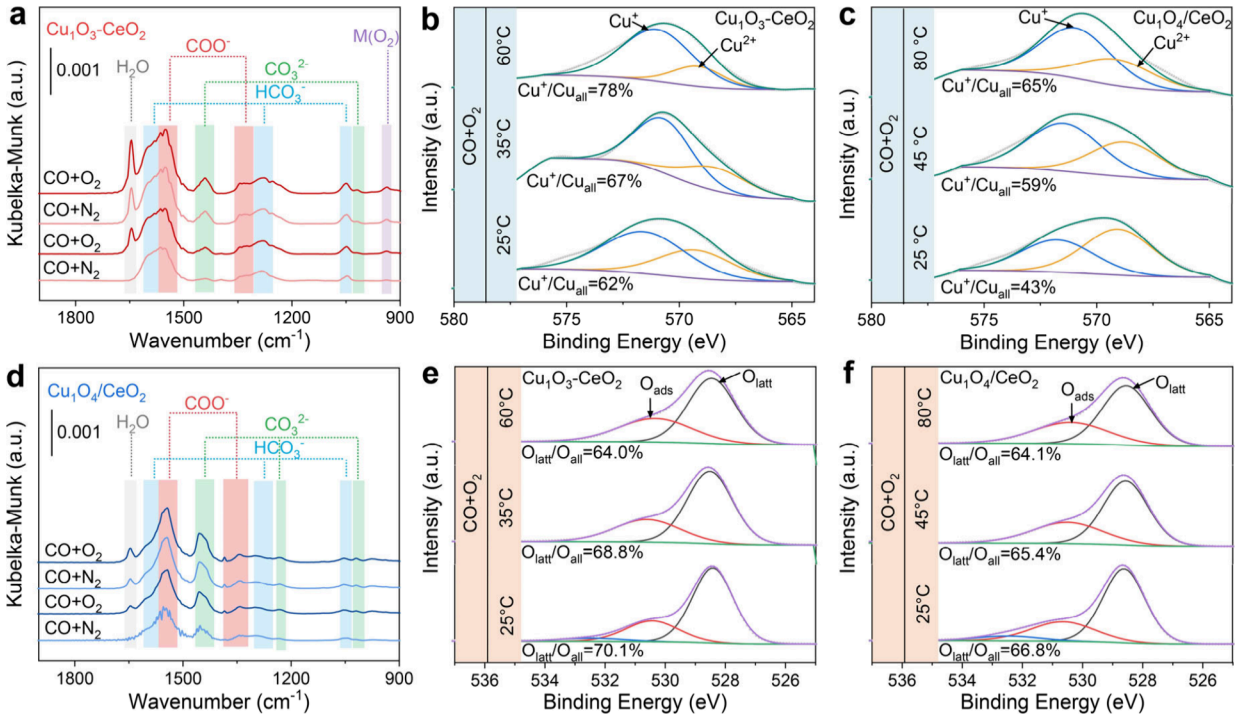

Figure 5. *In situ* DRIFTS of CO oxidation under various reaction conditions at (a) 65 °C over Cu_1O_3−CeO_2 and (d) 85 °C over Cu_1O_4/CeO_2 catalysts. Operando Cu LMM NAP-XPS spectra of (b) Cu_1O_3−CeO_2 and (c) Cu_1O_4/CeO_2 catalysts obtained from the CO oxidation process. Operando O 1*s* NAP-XPS spectra of (e) Cu_1O_3−CeO_2 and (f) Cu_1O_4/CeO_2 catalysts obtained from the CO oxidation process.

oxidation activity of the catalysts, suggesting that Cu atom sites play a pivotal role in enhancing CO adsorption.

Mechanism Study

The *in situ* DRIFTS measurements were recorded to further study the CO oxidation mechanism over the prepared catalysts. As shown in Figures S21−S23, the *in situ* temperature-programmed DRIFTS results reveal that bicarbonate species HCO_3* (1608 and 1049 cm^{-1}), formate species HCOO* (1550 and 1336 cm^{-1}), and carbonate species CO_3^{2-}* (1442 and 1016 cm^{-1}) are observed as intermediates in all three catalysts. There is an obvious enhancement of HCOO* (1550 and 1336 cm^{-1}) and CO_3^{2-}* (1442 and 1016 cm^{-1}) species as the temperature increasing.[23,57,58] Especially, when the reaction temperature was increased from 25 to 60 °C, the IR absorption peak of HCO_3* located at ∼1608 cm^{-1} shows conspicuous difference between Cu_1O_3−CeO_2 and Cu_1O_4/CeO_2 (Figures S21 and S22). The $CuCeO_x$ catalyst also exhibits similar intermediates as those of Cu_1O_3−CeO_2 due to partial Cu species doped into the bulk phases to form the bulk $Cu_yCe_{1-y}O_{2-x}$ solid solution (Figure S23). The results indicate that the formation of bicarbonate is facilitated when Cu species penetrate into the CeO_2 lattice, while Cu_1O_3−CeO_2 with atomic dispersion of Cu species decompose bicarbonate more rapidly. From DFT calculations, it is known that Cu_1O_3−CeO_2 generates bicarbonate with the lowest energy barrier (Figure S24). It is established that the changes in the catalyst structure affect the formation of surface intermediates. Moreover, the per-oxo or superoxo species formed facilely at oxygen vacancy sites, corresponding absorption peak of metal per-oxo complexes located at 937 cm^{-1} (ν_{O-O}) in Cu_1O_3−CeO_2 spectrum.[59−61] The electrons of the lattice oxygen are activated and transfer to the adjacent coordination-unsaturated copper species, resulting in charge separation and formation of Cu^+. Subsequently, the molecular oxygen species is protonated to form the metal per-oxy species $M(O_2)$ due to the proton transfer during the reaction, resulting in the weakened O−O bonding and fast activation of the oxygen molecules. The activated $*O_2^{2-}$ attacks one of the coordination bonds of CO to form $*CO_2$, which reacts with the polar group OH- to form the thermally less stable HCO_3* even at room temperature.[23,62,63] The desorption of intermediates was promoted, making it easier for Cu^+ to adsorb CO on its surface.

To further investigate the surface mechanisms, successive *in situ* DRIFTS were performed at T_{90} with the reaction atmosphere switched between air and nitrogen (Figures 5a,d, and S25). Previous studies suggested that the CO oxidation by the CeO_2-supported catalysts followed the MvK mechanism.[59,64−67] The Cu−Ce catalysts in this study also follow the MvK mechanism *via in situ* DRIFTS under the CO + N_2/O_2 conditions. The formation of the same type of intermediates both in an atmosphere of CO + N_2 or atmosphere of CO + O_2 provides powerful evidence that the lattice oxygen is the reactive oxygen species. Provided that no H_2O peak is observed in the *in situ* temperature-programmed DRIFTS, the reaction path can be derived as follows: in the absence of O_2, the intermediates accumulate when the reaction proceeds in CO + N_2 conditions; while in the presence of O_2, the intermediates accumulate rapidly and combine with the free proton to form H_2O. The production of H_2O is proportional to the production of the thermally less stable HCO_3^-, dominating in the Cu_1O_3−CeO_2 catalyst. Operando near ambient pressure XPS (NAP-XPS) measurements were conducted to obtain detailed information on the oxidation states of the catalyst components as well as the activation and transformation of oxygen species during the reaction. The fresh samples were analyzed according to the temperatures at room temperature, T_{50}, and T_{90}, respectively, detected from the CO

https://doi.org/10.1021/jacsau.4c01149
JACS Au 2025, 5, 1677−1688

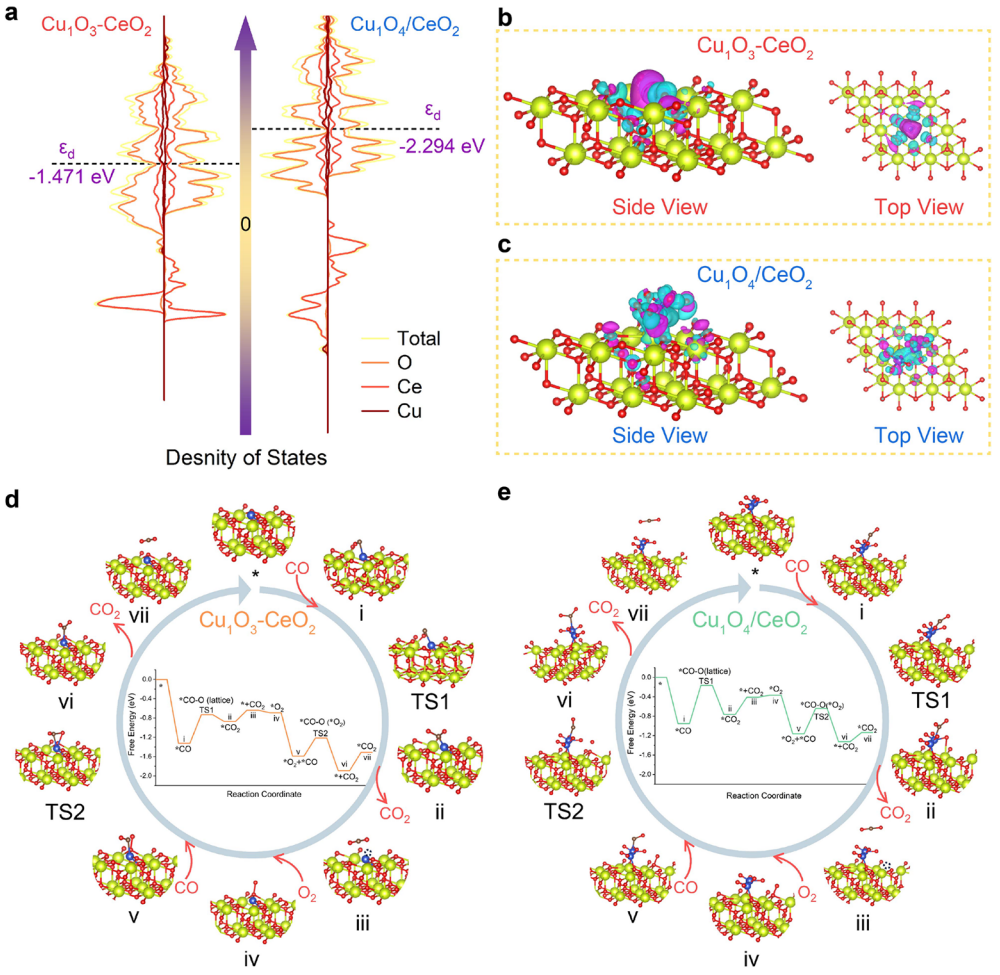

Figure 6. (a) Calculated total density of states (TDOS) and partial density of states (PDOS) of Cu_1O_3−CeO_2 and Cu_1O_4/CeO_2 catalysts. Calculated charge density differences of (b) Cu_1O_3−CeO_2 and (c) Cu_1O_4/CeO_2 catalysts; color code: Ce (Green), O (red), and Cu (blue). Proposed mechanisms of CO oxidation on (d) Cu_1O_3−CeO_2 and (e) Cu_1O_4/CeO_2 catalysts. "*" indicates initial state; "TS" indicates transition states. The reaction energies and activation energies are indicated in eV in the potential energy diagram. Color code: Ce (green), O (red), Cu (blue), and C (brown).

oxidation performance. The change in valence states of the Cu species during the CO oxidation process was detected, most probably due to the interaction between reducible oxides and metals and the presence of oxygen defects. Cu LMM indicates that Cu species are all maintained in the oxidized state, which are composed of Cu^{2+} evidenced by the peaks at 571.5 and Cu^{+} at 569.3 eV (Figure 5b,c).[34−36] When samples were treated in the reaction gas at reaction temperatures, Ce^{4+} is formed as a result of the addition of oxygen to the oxygen vacancy according to the kröger-vink equation,[68] resulting in the rapid reduction of Cu^{2+} to Cu^{+}. Subsequently, the concentration of Cu^{+} species on the support's surface continually increases with the increasing of temperature. Interestingly, the Cu_1O_3−CeO_2 catalyst exhibits a stronger electron transfer ability compared to the Cu_1O_4/CeO_2 catalyst with a much weaker electron transfer ability under the same conditions.

Moreover, a higher temperature was required to initiate the active Cu^{+} species of Cu_1O_4/CeO_2. These observations demonstrate that Cu^{+} in Cu−Ce catalysts is a superior site for activating CO molecules. The operando NAP-XPS results further confirm that the Cu−O bonds with coordination-unsaturated sites have a stronger electron transfer ability under the reaction atmosphere. The effect of Cu species on the charge density of CeO_2 was confirmed by a charge density distribution analysis. As shown in Figure 6b,c, the blue and purple isosurfaces correspond to the accumulating and depleting electron densities, respectively. The cutoff of density difference isosurface was equal to 0.005 eV·Å^{-3}. The local environment around the Cu sites leads to varying extents of charge transfer. We observed that Cu_1O_3−CeO_2 has a stronger electron transfer capability compared to Cu_1O_4/CeO_2. The Cu atom in a coordination-unsaturated state enhances the electron transfer to the uncoordinated O atom, which induces a shift of the electron cloud density toward the uncoordinated oxygen atom, resulting in facile activation of the oxygen atom in Cu_1−O_3.

Subsequently, the activation and transformation of oxygen species were investigated by operando 1*s* near ambient pressure XPS (NAP-XPS) (Figures 5e and 5f). The characteristic peaks around 528.4 and 530.4 eV were ascribed to the lattice oxygen (O_{latt}) and surface adsorbed oxygen (O_{ads}) species, respectively.[2,4,46] The peak located at 532.4 eV is assigned to the adsorbed H_2O groups on the catalyst surface.[50−52] Notably, the ratio of the O_{latt} species of the Cu_1O_3−CeO_2 catalyst gradually decreases from 70.1% (25 °C) to 68.8% at T_{50} and 64.0% at T_{90}. The Cu_1O_4/CeO_2 catalyst exhibits the same decreasing tendency (from 66.8% at 25 °C to

https://doi.org/10.1021/jacsau.4c01149
JACS Au 2025, 5, 1677−1688

65.4% at T_{50} and 64.1% at T_{90}), indicating that the lattice oxygen involved in the reaction is the reactive oxygen species. We established that Cu_1O_3 is comparatively easier to activate the lattice oxygen of the CeO_2 support and enhance the oxygen transport in the Cu_1O_3−CeO_2 body phase to improve the reaction performance.

The ^{18}O isotopic labeling experiment was conducted to further explain the reaction mechanism of the catalysts (Figures S26 and S27). For the Cu_1O_3−CeO_2 and Cu_1O_4/CeO_2 catalysts, the signal of $C^{16}O_2$ species (m/z = 44) increased rapidly with the increasing of reaction temperature, and the signal of this species was significantly higher than that of $C^{16}O^{18}O$ species (m/z = 46) and $C^{18}O_2$ species (m/z = 48), due to the consumption of lattice oxygen species over catalysts surface, further proving that the CO oxidation over Cu_1O_3−CeO_2 and Cu_1O_4/CeO_2 catalysts followed the MvK mechanism. In addition, it can be observed that Cu_1O_3−CeO_2 catalyst possesses the higher $C^{16}O_2$ signal at low-temperatures than Cu_1O_4/CeO_2 catalyst, indicating that the atomically dispersed unsaturated coordination site of Cu_1O_3−CeO_2 promotes the activation of lattice oxygens and improves the catalytic performance.

DFT calculations were conducted to simulate the approximate structure of the Cu atoms on the CeO_2 surface based on the EXAFS fitting results, where the {111} plane of CeO_2 is dominantly exposed, as derived from HR-TEM results (Figures 2a and 2b). The calculated total density of states (TDOS) and projected density of states (PDOS) reveal that the energy levels around the Cu_1O_3−CeO_2 Fermi level are continuous, with no band gap (Figure 6a). The *d*-band center (ε_d, the average position of the d-orbital of metal atom) of the Cu_1O_3−CeO_2 catalyst was calculated to be −1.471 eV, which is much closer to the Fermi level (0 eV), indicating a higher electron transport ability and an increased activation effect on the contaminant. The higher number of electrons in the Fermi energy level is mainly due to the presence of Cu atom, which lead to a change in the energy level of Ce atom and an enhancement of the Cu−O coupling.

The reaction mechanisms of CO oxidation over Cu_1O_3−CeO_2 and Cu_1O_4/CeO_2 are illustrated in Figures 6d and 6e. The results are derived from the Mars−van Krevelen (MvK) mechanism, which is based on the analysis of *in situ* DRIFTS, operando NAP-XPS data, and an ^{18}O isotopic labeling experiment. For Cu_1O_3−CeO_2, the surface adsorbed CO with a lower free energy (−1.32 eV) tends to be adsorbed on the coordination-unsaturated site of copper, resulting in forming a four-coordination configuration first (structure (i). Next, the activation energies of *CO during reaction with lattice oxygens (TS1) of Cu_1O_3−CeO_2 and Cu_1O_4/CeO_2 were calculated as 0.59 and 0.82 eV, respectively. Similarly, the lattice oxygens next to Cu_1−O_3 and at the interface are activated in two catalysts. The low barrier energy of the lattice oxygen during reaction with CO leads to the efficient conversion under low temperature of CO oxidation reaction. The desorption energy of physically adsorbed *CO_2 on the surface (structure (ii), is found to be 0.23 eV on Cu_1O_3−CeO_2. We propose that an oxygen vacancy is formed at the interface, and a bare Cu site is exposed after the release of the first CO_2 (structure (iii), followed by the adsorption of *O_2 on oxygen vacancy (iv). CO adsorbs continuously on Cu species; whereas, the oxygen vacancy is directly involved in the formation of the second molecular CO_2, with decreases apparent activation energy values of 0.52 and 0.37 eV (TS2) over Cu_1O_4/CeO_2 and Cu_1O_3−CeO_2 catalysts, respectively. Finally, the catalytic oxidation cycle is completed after the dissociation of *CO_2. The rate-determining step of CO oxidation over the prepared catalyst is determined as the surface reaction between CO and lattice oxygen or adsorbed oxygen.

CONCLUSIONS

This study employed various bonding methods to deliberately manipulate the Cu species on the CeO_2 supports, resulting in a broad range of atomic Cu sites and, consequently, a different range of reaction mechanisms. The incorporation of adequate quantities of Cu into CeO_2 established extensively distributed coordination-unsaturated Cu sites. In comparison to the traditional Cu−Ce catalyst, the Cu_1O_3−CeO_2 catalyst possesses a higher amount of Cu^+ as a CO adsorption site and rapidly activated lattice oxygen as reactive oxygen species. According to *in situ* DRIFTS data, metal peroxides are formed at coordination-unsaturated Cu_1−O_3 sites, which then attack the reactant coordination bonds and desorb the intermediates quickly. We propose that the atomic Cu sites with coordination-unsaturated state leads to electron cloud density migration from the uncoordinated Cu atoms to O atoms. Subsequently, the transfer of electrons from O atoms to Cu species upon activation of lattice oxygen dominates in charge separation and promotes the generation of Cu^+ and per-oxy species, thereby enhancing the surface reaction of active oxygen species with CO. We propose that the activation of oxygen species and modulation of metal active centers may be improved by constructing highly distributed coordination-unsaturated copper sites using a doping approach, leading to superb catalytic oxidation performance.

ASSOCIATED CONTENT

Supporting Information

The Supporting Information is available free of charge at https://pubs.acs.org/doi/10.1021/jacsau.4c01149.

Detailed information on the preparation of catalysts, catalyst characterizations, catalytic performance evaluation, *in situ* DRIFTS, NAP-XPS, theoretical studies, and supplementary figures and tables (PDF)

AUTHOR INFORMATION

Corresponding Authors

Hongna Zhang − *CAS Research/Education Center for Excellence in Molecular Sciences, Institute of Chemistry, Chinese Academy of Sciences, Beijing 100190, P.R. China*; Email: lxiaon1124@gmail.com

Chi He − *State Key Laboratory of Multiphase Flow in Power Engineering, School of Energy and Power Engineering, Xi'an Jiaotong University, Xi'an 710049 Shaanxi, P.R. China; National Engineering Laboratory for VOCs Pollution Control Material & Technology, University of Chinese Academy of Sciences, Beijing 101408, P.R. China*; orcid.org/0000-0001-6403-1277; Email: chi_he@xjtu.edu.cn

Authors

Yadi Wang − *State Key Laboratory of Multiphase Flow in Power Engineering, School of Energy and Power Engineering, Xi'an Jiaotong University, Xi'an 710049 Shaanxi, P.R. China; Key Laboratory of Subsurface Hydrology and*

https://doi.org/10.1021/jacsau.4c01149
JACS Au 2025, 5, 1677−1688

Ecological Effects in Arid Region, Ministry of Education, School of Water and Environment, Chang'an University, Xi'an 710064, P.R. China

Zeyu Jiang − *State Key Laboratory of Multiphase Flow in Power Engineering, School of Energy and Power Engineering, Xi'an Jiaotong University, Xi'an 710049 Shaanxi, P.R. China;* orcid.org/0000-0002-9997-2357

Fan Dang − *State Key Laboratory of Multiphase Flow in Power Engineering, School of Energy and Power Engineering, Xi'an Jiaotong University, Xi'an 710049 Shaanxi, P.R. China*

Chaoqian Ai − *State Key Laboratory of Multiphase Flow in Power Engineering, School of Energy and Power Engineering, Xi'an Jiaotong University, Xi'an 710049 Shaanxi, P.R. China;* orcid.org/0009-0005-6928-7526

Jialei Wan − *State Key Laboratory of Multiphase Flow in Power Engineering, School of Energy and Power Engineering, Xi'an Jiaotong University, Xi'an 710049 Shaanxi, P.R. China*

Chunli Ai − *State Key Laboratory of Multiphase Flow in Power Engineering, School of Energy and Power Engineering, Xi'an Jiaotong University, Xi'an 710049 Shaanxi, P.R. China*

Yani Wu − *State Key Laboratory of Multiphase Flow in Power Engineering, School of Energy and Power Engineering, Xi'an Jiaotong University, Xi'an 710049 Shaanxi, P.R. China*

Chi Ma − *State Key Laboratory of Multiphase Flow in Power Engineering, School of Energy and Power Engineering, Xi'an Jiaotong University, Xi'an 710049 Shaanxi, P.R. China*

Mingjiao Tian − *State Key Laboratory of Multiphase Flow in Power Engineering, School of Energy and Power Engineering, Xi'an Jiaotong University, Xi'an 710049 Shaanxi, P.R. China*

Han Xu − *State Key Laboratory of Multiphase Flow in Power Engineering, School of Energy and Power Engineering, Xi'an Jiaotong University, Xi'an 710049 Shaanxi, P.R. China*

Reem Albilali − *Department of Chemistry, College of Science, Imam Abdulrahman Bin Faisal University, Dammam 31441, Saudi Arabia*

Weisheng Guan − *Key Laboratory of Subsurface Hydrology and Ecological Effects in Arid Region, Ministry of Education, School of Water and Environment, Chang'an University, Xi'an 710064, P.R. China*

Complete contact information is available at: https://pubs.acs.org/10.1021/jacsau.4c01149

Author Contributions

[¶]Y.W., Z.J., and F.D. contributed equally to this work.

Author Contributions

C.H. conceived the experiments, supervised the project and conducted the data curation. Y.W. and Z.J. performed the catalysts preparation and catalytic evaluation. Material characterizations were performed by Y.W., Z.J., F.D., and Y.W. Data analysis support was done by J.W. and C.A. Following, C.M., M.T., and H.Z. performed the operando experiments. H.X. and W.G. contributed to the theoretical studies and assisted with analyzing the results. Writing was done by Y.W., Z.J., R.A., H.Z., and C.H. All authors have given approval to the final version of the article.

Notes

The authors declare no competing financial interest.

■ ACKNOWLEDGMENTS

This work was financially supported by the National Natural Science Foundation of China (22476157, 22406146, 22276145), the National Key R&D Program of China (2022YFB4101500), and the China Postdoctoral Science Foundation (2023M732783). The authors gratefully acknowledge the supports from instrumental analysis center of Xi'an Jiaotong University.

■ REFERENCES

(1) Yan, H.; Liu, B.; Zhou, X.; Meng, F.; Zhao, M.; Pan, Y.; Li, J.; Wu, Y.; Zhao, H.; Liu, Y.; Chen, X.; Li, L.; Feng, X.; Chen, D.; Shan, H.; Yang, C.; Yan, N. Enhancing Polyol/Sugar Cascade Oxidation to Formic Acid with Defect Rich MnO_2 Catalysts. *Nat. Commun.* **2023**, *14* (1), 4509.

(2) Chen, Y.; Lin, J.; Pan, Q.; Liu, X.; Ma, T.; Wang, X. Inter-Metal Interaction of Dual-Atom Catalysts in Heterogeneous Catalysis. *Angew. Chem., Int. Ed.* **2023**, *62* (42), No. e202306469.

(3) Yang, H.; Wang, X.; Liu, Q.; Huang, A.; Zhang, X.; Yu, Y.; Zhuang, Z.; Li, G.; Li, Y.; Peng, Q.; Chen, X.; Xiao, H.; Chen, C. Heterogeneous Iridium Single-Atom Molecular-like Catalysis for Epoxidation of Ethylene. *J. Am. Chem. Soc.* **2023**, *145* (12), 6658−6670.

(4) Jiang, Z.; Tian, M.; Jing, M.; Chai, S.; Jian, Y.; Chen, C.; Douthwaite, M.; Zheng, L.; Ma, M.; Song, W.; Liu, J.; Yu, J.; He, C. Modulating the Electronic Metal-Support Interactions in Single-Atom Pt_1-CuO Catalyst for Boosting Acetone Oxidation. *Angew. Chem., Int. Ed.* **2022**, *61* (28), No. e202200763.

(5) Zhang, J.; Zhang, Q.; Feng, X. Support and Interface Effects in Water-Splitting Electrocatalysts. *Adv. Mater.* **2019**, *31* (31), No. e1808167.

(6) Pu, T.; Zhang, W.; Zhu, M. Engineering Heterogeneous Catalysis with Strong Metal-Support Interactions: Characterization, Theory and Manipulation. *Angew. Chem., Int. Ed.* **2023**, *62* (4), No. e202212278.

(7) Liu, P.; Men, Y. L.; Meng, X. Y.; Peng, C.; Zhao, Y.; Pan, Y. X. Electronic Interactions on Platinum/(Metal-Oxide)-Based Photocatalysts Boost Selective Photoreduction of CO_2 to CH_4. *Angew. Chem., Int. Ed.* **2023**, *62* (38), No. e202309443.

(8) Su, J.; Ge, R.; Jiang, K.; Dong, Y.; Hao, F.; Tian, Z.; Chen, G.; Chen, L. Assembling Ultrasmall Copper-Doped Ruthenium Oxide Nanocrystals into Hollow Porous Polyhedra: Highly Robust Electrocatalysts for Oxygen Evolution in Acidic Media. *Adv. Mater.* **2018**, *30* (29), No. e1801351.

(9) Muravev, V.; Spezzati, G.; Su, Y.-Q.; Parastaev, A.; Chiang, F.-K.; Longo, A.; Escudero, C.; Kosinov, N.; Hensen, E. J. M. Interface Dynamics of Pd−CeO_2 Single-Atom Catalysts during CO Oxidation. *Nat. Catal.* **2021**, *4* (6), 469−478.

(10) Zhang, R.; Liu, G.; Huo, C.; Liu, J.; Zhang, B.; Yang, B.; Tian, X.; Wu, Z. Tailoring Catalytic and Oxygen Release Capability in $LaFe_{1-x}NixO_3$ to Intensify Chemical Looping Reactions at Medium Temperatures. *ACS Catal.* **2024**, *14* (10), 7771−7787.

(11) Wang, Y.; Zhu, B.; Sin, S.; Zhang, Z.; Tan, C.; Gu, Z.; Song, W.; Huang, C.; Tao, M.; Zhang, C.; Tang, C.; Dong, L. Lattice Oxygen Activation Triggered by Ultrasonic Shock Significantly Improves NO Selective Catalytic Reduction. *ACS Catal.* **2024**, *14* (12), 9265−9274.

(12) Liu, J.; Wang, T.; Sun, M.; Liao, M.; Wang, S.; Liu, S.; Shi, H.; Liu, Y.; Shen, Y.; Cao, R.; Huang, Y.; Huang, B.; Li, Q. Triggering the Dual-Metal-Site Lattice Oxygen Mechanism with In Situ-Generated Mn^{3+} Sites for Enhanced Acidic Oxygen Evolution. *J. Am. Chem. Soc.* **2024**, *146* (48), 33276−33287.

(13) Jiang, C.; Song, H.; Sun, G.; Chang, X.; Zhen, S.; Wu, S.; Zhao, Z. J.; Gong, J. Data-Driven Interpretable Descriptors for the Structure-Activity Relationship of Surface Lattice Oxygen on Doped Vanadium Oxides. *Angew. Chem., Int. Ed.* **2022**, *61* (35), No. e202206758.

(14) Qian, J.; Liu, X.; Zhong, C.; Xu, G.; Li, H.; Zhou, W.; You, B.; Wang, F.; Gao, D.; Chao, D. Enhanced Stability and Narrowed D-Band Gap of Ce-Doped Co_3O_4 for Rechargeable Aqueous Zn-Air Battery. *Adv. Funct. Mater.* **2023**, *33* (9), No. 2212021.

(15) Choi, S.; Kim, S. J.; Han, S.; Wang, J.; Kim, J.; Koo, B.; Ryabin, A. A.; Kunze, S.; Hyun, H.; Han, J.; Haw, S. C.; Chae, K. H.; Choi, C. H.; Kim, H.; Lim, J. Enhancing Oxygen Evolution Reaction via a Surface Reconstruction-Induced Lattice Oxygen Mechanism. *ACS Catal.* **2024**, *14* (20), 15096−15107.
(16) Yin, Y.; Luo, B.; Sun, Y.; Xie, P.; Xiong, H.; Zhu, T.; Li, X. Activation of Lattice Oxygen in Ceria by Plasma Exsolution of MoO_x with Atomic Dispersion for NO_x Abatement. *ACS Catal.* **2024**, *14* (7), 5236−5246.
(17) Liu, H. X.; Li, S. Q.; Wang, W. W.; Yu, W. Z.; Zhang, W. J.; Ma, C.; Jia, C. J. Partially Sintered Copper−Ceria as Excellent Catalyst for the High-Temperature Reverse Water Gas Shift Reaction. *Nat. Commun.* **2022**, *13* (1), 867.
(18) Hong, S.; Abbas, H. G.; Jang, K.; Patra, K. K.; Kim, B.; Choi, B. U.; Song, H.; Lee, K. S.; Choi, P. P.; Ringe, S.; Oh, J. Tuning the C_1/C_2 Selectivity of Electrochemical CO_2 Reduction on Cu-CeO_2 Nanorods by Oxidation State Control. *Adv. Mater.* **2023**, *35* (8), No. e2208996.
(19) Sun, Y.; Polo-Garzon, F.; Bao, Z.; Moon, J.; Huang, Z.; Chen, H.; Chen, Z.; Yang, Z.; Chi, M.; Wu, Z.; Liu, J.; Dai, S. Manipulating Copper Dispersion on Ceria for Enhanced Catalysis: A Nanocrystal-Based Atom-Trapping Strategy. *Adv. Sci.* **2022**, *9* (8), No. e2104749.
(20) Zhou, X.; Shan, J.; Chen, L.; Xia, B. Y.; Ling, T.; Duan, J.; Jiao, Y.; Zheng, Y.; Qiao, S. Z. Stabilizing Cu^{2+} Ions by Solid Solutions to Promote CO_2 Electroreduction to Methane. *J. Am. Chem. Soc.* **2022**, *144* (5), 2079−2084.
(21) Wang, F.; Tian, J.; Li, M.; Li, W.; Chen, L.; Liu, X.; Li, J.; Muhetaer, A.; Li, Q.; Wang, Y.; Gu, L.; Ma, D.; Xu, D. A Photoactivated Cu-CeO_2 Catalyst with Cu-[O]-Ce Active Species Designed through MOF Crystal Engineering. *Angew. Chem., Int. Ed.* **2020**, *59* (21), 8203−8209.
(22) Wang, W. W.; Du, P. P.; Zou, S. H.; He, H. Y.; Wang, R. X.; Jin, Z.; Shi, S.; Huang, Y. Y.; Si, R.; Song, Q. S.; Jia, C. J.; Yan, C. H. Highly Dispersed Copper Oxide Clusters as Active Species in Copper-Ceria Catalyst for Preferential Oxidation of Carbon Monoxide. *ACS Catal.* **2015**, *5* (4), 2088−2099.
(23) Wang, W. W.; Yu, W. Z.; Du, P. P.; Xu, H.; Jin, Z.; Si, R.; Ma, C.; Shi, S.; Jia, C. J.; Yan, C. H. Crystal Plane Effect of Ceria on Supported Copper Oxide Cluster Catalyst for CO Oxidation: Importance of Metal−Support Interaction. *ACS Catal.* **2017**, *7* (2), 1313−1329.
(24) Kang, L.; Wang, B.; Bing, Q.; Zalibera, M.; Buchel, R.; Xu, R.; Wang, Q.; Liu, Y.; Gianolio, D.; Tang, C. C.; Gibson, E. K.; Danaie, M.; Allen, C.; Wu, K.; Marlow, S.; Sun, L. D.; He, Q.; Guan, S.; Savitsky, A.; Velasco-Velez, J. J.; Callison, J.; Kay, C. W. M.; Pratsinis, S. E.; Lubitz, W.; Liu, J. Y.; Wang, F. R. Adsorption and Activation of Molecular Oxygen over Atomic Copper(I/II) Site on Ceria. *Nat. Commun.* **2020**, *11* (1), 4008.
(25) Patra, K. K.; Liu, Z.; Lee, H.; Hong, S.; Song, H.; Abbas, H. G.; Kwon, Y.; Ringe, S.; Oh, J. Boosting Electrochemical CO_2 Reduction to Methane via Tuning Oxygen Vacancy Concentration and Surface Termination on a Copper/Ceria Catalyst. *ACS Catal.* **2022**, *12* (17), 10973−10983.
(26) Elias, J. S.; Artrith, N.; Bugnet, M.; Giordano, L.; Botton, G. A.; Kolpak, A. M.; Shao-Horn, Y. Elucidating the Nature of the Active Phase in Copper/Ceria Catalysts for CO Oxidation. *ACS Catal.* **2016**, *6* (3), 1675−1679.
(27) Elias, J. S.; Stoerzinger, K. A.; Hong, W. T.; Risch, M.; Giordano, L.; Mansour, A. N.; Shao-Horn, Y. In Situ Spectroscopy and Mechanistic Insights into CO Oxidation on Transition-Metal-Substituted Ceria Nanoparticles. *ACS Catal.* **2017**, *7* (10), 6843−6857.
(28) Elias, J. S.; Risch, M.; Giordano, L.; Mansour, A. N.; Shao-Horn, Y. Structure, bonding, and catalytic activity of monodisperse, transition-metal-substituted CeO_2 nanoparticles. *J. Am. Chem. Soc.* **2014**, *136* (49), 17193−17200.
(29) Yu, W. Z.; Wang, W. W.; Li, S. Q.; Fu, X. P.; Wang, X.; Wu, K.; Si, R.; Ma, C.; Jia, C. J.; Yan, C. H. Construction of Active Site in a Sintered Copper-Ceria Nanorod Catalyst. *J. Am. Chem. Soc.* **2019**, *141* (44), 17548−17557.
(30) Chen, Z.; Liu, Z.; Xu, X. Dynamic Evolution of the Active Center Driven by Hemilabile Coordination in Cu/CeO_2 Single-Atom Catalyst. *Nat. Commun.* **2023**, *14* (1), 2512.
(31) Yun, Y.; Zeng, H.; Li, L.; Li, H.; Cheng, S.; Sun, N.; Li, M.; Sheng, H.; Hu, S.; Yao, T.; Zhu, M. Matching Bidentate Ligand Anchoring: an Accurate Control Strategy for Stable Single-Atom/ZIF Nanocatalysts. *Adv. Mater.* **2023**, *35* (7), No. e2209561.
(32) Jiang, X.; Tang, L.; Dong, L.; Sheng, X.; Zhang, W.; Liu, Z.; Shen, J.; Jiang, H.; Li, C. Cu Single-Atom Catalysts for High-Selectivity Electrocatalytic Acetylene Semihydrogenation. *Angew. Chem., Int. Ed.* **2023**, *62* (33), No. e202307848.
(33) Dong, J.; Liu, Y.; Pei, J.; Li, H.; Ji, S.; Shi, L.; Zhang, Y.; Li, C.; Tang, C.; Liao, J.; Xu, S.; Zhang, H.; Li, Q.; Zhao, S. Continuous Electroproduction of Formate via CO_2 Reduction on Local Symmetry-Broken Single-Atom Catalysts. *Nat. Commun.* **2023**, *14* (1), 6849.
(34) Lv, J.; Li, W.; Li, J.; Zhu, Z.; Dong, A.; Lv, H.; Li, P.; Wang, B. A Triptycene-Based 2D MOF with Vertically Extended Structure for Improving the Electrocatalytic Performance of CO_2 to Methane. *Angew. Chem., Int. Ed.* **2023**, *62* (11), No. e202217958.
(35) Zhao, P.; Jiang, H.; Shen, H.; Yang, S.; Gao, R.; Guo, Y.; Zhang, Q.; Zhang, H. Construction of Low-Coordination Cu-C_2 Single-Atoms Electrocatalyst Facilitating the Efficient Electrochemical CO_2 Reduction to Methane. *Angew. Chem., Int. Ed.* **2023**, *62* (49), No. e202314121.
(36) Zhang, Y.; Dong, L. Z.; Li, S.; Huang, X.; Chang, J. N.; Wang, J. H.; Zhou, J.; Li, S. L.; Lan, Y. Q. Coordination Environment Dependent Selectivity of Single-Site-Cu Enriched Crystalline Porous Catalysts in CO_2 Reduction to CH_4. *Nat. Commun.* **2021**, *12* (1), 6390.
(37) Kelly, K. L.; Coronado, E.; Zhao, L. L.; Schatz, G. C. The Optical Properties of Metal Nanoparticles: The Influence of Size, Shape, and Dielectric Environment. *J. Phys. Chem. B* **2003**, *107* (3), 668−677.
(38) Zhang, T.; Li, J.; Liu, J.; Wang, D.; Zhao, Z.; Cheng, K.; Li, J. High Activity and Wide Temperature Window of Fe-Cu-SSZ-13 in the Selective Catalytic Reduction of NO with Ammonia. *AIChE J.* **2015**, *61* (11), 3825−3837.
(39) Fan, C.; Chen, Z.; Pang, L.; Ming, S.; Zhang, X.; Albert, K. B.; Liu, P.; Chen, H.; Li, T. The Influence of Si/Al Ratio on the Catalytic Property and Hydrothermal Stability of Cu-SSZ-13 Catalysts for NH_3-SCR. *Appl. Catal. A-Gen.* **2018**, *550*, 256−265.
(40) Fan, C.; Chen, Z.; Pang, L.; Ming, S.; Dong, C.; Brou Albert, K.; Liu, P.; Wang, J.; Zhu, D.; Chen, H.; Li, T. Steam and Alkali Resistant Cu-SSZ-13 Catalyst for the Selective Catalytic Reduction of NO_x in Diesel Exhaust. *Chem. Eng. J.* **2018**, *334*, 344−354.
(41) Chen, M.; Li, J.; Xue, W.; Wang, S.; Han, J.; Wei, Y.; Mei, D.; Li, Y.; Yu, J. Unveiling Secondary-Ion-Promoted Catalytic Properties of Cu-SSZ-13 Zeolites for Selective Catalytic Reduction of NO_x. *J. Am. Chem. Soc.* **2022**, *144* (28), 12816−12824.
(42) Jiang, W. J.; Yin, Y.; Liu, X. Q.; Yin, X. Q.; Shi, Y. Q.; Sun, L. B. Fabrication of Supported Cuprous Sites at Low Temperatures: an Efficient, Controllable Dtrategy using Vapor-Induced Reduction. *J. Am. Chem. Soc.* **2013**, *135* (22), 8137−8140.
(43) Peerlings, M. L. J.; Han, K.; Longo, A.; Helfferich, K. H.; Ghiasi, M.; de Jongh, P. E.; Ngene, P. Synthesis and Catalytic Performance of Bimetallic Oxide-Derived CuO−ZnO Electrocatalysts for CO2 Reduction. *ACS Catal.* **2024**, *14* (14), 10701−10711.
(44) Zhao, Y.; Zhang, B.; Xia, B.; Liu, Z.; Tan, C.; Song, C.; Fujii, M.; Ma, L.; Song, M. Defect Engineering Boosted Peroxydisulfate Activation of Dual-Vacancy Cu−Fe Spinel Oxides for Soil Organics Decontamination. *ACS ES&T Engg.* **2024**, *4* (8), 2025−2035.
(45) Xu, J.; Zhang, Y.; Xu, X.; Fang, X.; Xi, R.; Liu, Y.; Zheng, R.; Wang, X. Constructing $La_2B_2O_7$ (B = Ti, Zr, Ce) Compounds with Three Typical Crystalline Phases for the Oxidative Coupling of Methane: The Effect of Phase Structures, Superoxide Anions, and Alkalinity on the Reactivity. *ACS Catal.* **2019**, *9* (5), 4030−4045.

https://doi.org/10.1021/jacsau.4c01149
JACS Au 2025, 5, 1677−1688

(46) Xu, X.; Liu, L.; Tong, Y.; Fang, X.; Xu, J.; Jiang, D.-e.; Wang, X. Facile Cr^{3+}-Doping Strategy Dramatically Promoting Ru/CeO_2 for Low-Temperature CO_2 Methanation: Unraveling the Roles of Surface Oxygen Vacancies and Hydroxyl Groups. *ACS Catal.* **2021**, *11* (9), 5762−5775.
(47) Ai, C.; Wang, B.; Duan, K.; Jiang, J.; Jiang, Z.; Hu, S.; Luo, B.; Ma, L.; Jing, D. Enhanced Photocatalytic Activity by Regulating Charge Transferring: Unveiling the Decisive Role of Cerium Oxide Crystal-Facet Engineering over Heterojunction. *J. Colloid Interface Sci.* **2023**, *636*, 341−350.
(48) Liao, Y.; Liu, Z.; Li, Z.; Gao, G.; Ji, L.; Xu, H.; Huang, W.; Qu, Z.; Yan, N. The Unique CO Activation Effects for Boosting NH_3 Selective Catalytic Oxidation over CuO_x-CeO_2. *Environ. Sci. Technol.* **2022**, *56* (14), 10402−10411.
(49) Chen, Y.; Ji, S.; Sun, W.; Chen, W.; Dong, J.; Wen, J.; Zhang, J.; Li, Z.; Zheng, L.; Chen, C.; Peng, Q.; Wang, D.; Li, Y. Discovering Partially Charged Single-Atom Pt for Enhanced Anti-Markovnikov Alkene Hydrosilylation. *J. Am. Chem. Soc.* **2018**, *140* (24), 7407−7410.
(50) Shen, Y.; Deng, J.; Impeng, S.; Li, S.; Yan, T.; Zhang, J.; Shi, L.; Zhang, D. Boosting Toluene Combustion by Engineering Co-O Strength in Cobalt Oxide Catalysts. *Environ. Sci. Technol.* **2020**, *54* (16), 10342−10350.
(51) Wang, M.; Zhang, Y.; Yu, Y.; Shan, W.; He, H. Synergistic Effects of Multicomponents Produce Outstanding Soot Oxidation Activity in a $Cs/Co/MnO_x$ Catalyst. *Environ. Sci. Technol.* **2021**, *55* (1), 240−248.
(52) Xiang, L.; Lin, F.; Cai, B.; Wang, K.; Wang, Z.; Yan, B.; Chen, G.; He, C. Evaluation of the Flexibility for Catalytic Ozonation of Dichloromethane over Urchin-Like $CuMnO_x$ in Flue Gas with Complicated Components. *Environ. Sci. Technol.* **2022**, *56* (18), 13379−13390.
(53) Zeng, M.; Li, Y.; Mao, M.; Bai, J.; Ren, L.; Zhao, X. Synergetic Effect between Photocatalysis on TiO_2 and Thermocatalysis on CeO_2 for Gas-Phase Oxidation of Benzene on TiO_2/CeO_2 Nanocomposites. *ACS Catal.* **2015**, *5* (6), 3278−3286.
(54) Zhou, Y.; Wang, Z.; Liu, C. Perspective on CO Oxidation over Pd-Based Catalysts. *Catal. Sci. Technol.* **2015**, *5* (1), 69−81.
(55) Ren, P.; Tu, W.; Wang, C.; Cheng, S.; Liu, W.; Zhang, Z.; Tian, Y.; Han, Y. F. Mechanism and Sites Requirement for CO Hydrogenation to CH_3OH over Cu/CeO_2 Catalysts. *Appl. Catal., B* **2022**, *305*, No. 121016.
(56) Dai, L.; Li, B.; Peng, Y.; Hao, X.; Xuan, R.; Huang, H.; Bi, Y.; Xu, L.; Zhang, Y.; Guo, Y.; Du, F.; Wang, L.; Wang, H. Tuning Interaction Strength between CeO_2 and Iridium to Promote CO Oxidation over Ir/TiO_2. *J. Rare Earth.* **2024**, *42* (4), 651−659.
(57) Hazlett, M. J.; Moses-Debusk, M.; Parks, J. E.; Allard, L. F.; Epling, W. S. Kinetic and Mechanistic Study of Bimetallic Pt-Pd/Al_2O_3 Catalysts for CO and C_3H_6 Oxidation. *Appl. Catal., B* **2017**, *202*, 404−417.
(58) Zhang, S.; Li, X. S.; Chen, B.; Zhu, X.; Shi, C.; Zhu, A. M. CO Oxidation Activity at Room Temperature over Au/CeO_2 Catalysts: Disclosure of Induction Period and Humidity Effect. *ACS Catal.* **2014**, *4* (10), 3481−3489.
(59) Liu, M. H.; Chen, Y. W.; Lin, T. S.; Mou, C. Y. Defective Mesocrystal ZnO-Supported Gold Catalysts: Facilitating CO Oxidation via Vacancy Defects in ZnO. *ACS Catal.* **2018**, *8* (8), 6862−6869.
(60) Bongiorno, A.; Landman, U. Water-Enhanced Catalysis of CO Oxidation on Free and Supported Gold Nanoclusters. *Phys. Rev. Lett.* **2005**, *95* (10), No. 106102.
(61) Tran-Thuy, T. M.; Chen, C. C.; Lin, S. D. Spectroscopic Studies of How Moisture Enhances CO Oxidation over Au/BN at Ambient Temperature. *ACS Catal.* **2017**, *7* (7), 4304−4312.
(62) Davó-Quiñonero, A.; Navlani-García, M.; Lozano-Castelló, D.; Bueno-López, A.; Anderson, J. A. Role of Hydroxyl Groups in the Preferential Oxidation of CO over Copper Oxide−Cerium Oxide Catalysts. *ACS Catal.* **2016**, *6* (3), 1723−1731.
(63) Chen, D.; Su, Z.; Si, W.; Qu, Y.; Zhao, X.; Liu, H.; Yang, Y.; Wang, Y.; Peng, Y.; Chen, J.; Li, J. Boosting CO Catalytic Oxidation Performance via Highly Dispersed Copper Atomic Clusters: Regulated Electron Interaction and Reaction Pathways. *Environ. Sci. Technol.* **2023**, *57* (7), 2928−2938.
(64) Xing, Y.; Wang, C.; Li, D.; Wang, R.; Liang, S.; Li, Y.; Liu, Y.; Zhang, X. Solution Plasma Processing Single-Atom Au_1 on CeO_2 Nanosheet for Low Temperature Photo-Enhanced Mars−van Krevelen CO Oxidation. *Adv. Funct. Mater.* **2022**, *32* (48), No. 2207694.
(65) Kim, H. J.; Jang, M. G.; Shin, D.; Han, J. W. Design of Ceria Catalysts for Low-Temperature CO Oxidation. *ChemCatChem.* **2020**, *12* (1), 11−26.
(66) Bac, S.; Mallikarjun Sharada, S. CO Oxidation with Atomically Dispersed Catalysts: Insights from the Energetic Span Model. *ACS Catal.* **2022**, *12* (3), 2064−2076.
(67) Wang, Y. G.; Cantu, D. C.; Lee, M. S.; Li, J.; Glezakou, V. A.; Rousseau, R. CO Oxidation on Au/TiO_2: Condition-Dependent Active Sites and Mechanistic Pathways. *J. Am. Chem. Soc.* **2016**, *138* (33), 10467−10476.
(68) Ai, C.; Shi, J.; Hu, S.; Li, J.; Luo, B.; Jing, D. Morphologies Dependence of Hydrogen Evolution over CeO_2 via Ultrasonic Triggering. *Int. J. Hydrogen Energy* **2022**, *47* (34), 15149−15159.

https://doi.org/10.1021/jacsau.4c01149
JACS Au 2025, 5, 1677−1688